Influence of Receptivity on Subharmonic Transition by Tollmien-Schlichting Waves

M. Kim* and I. Sohn*
Corresponding author: sohniy@kisti.re.kr
* Korea Institute of Science and Technology Information, Korea.

Abstract: Turbulent transition predictions often focus on growth of isolated unstable modes and typically neglect the receptivity stage. Consequently, the effects of coexisting modes generated during receptivity on nonlinear breakdown remain under-investigated. This study addresses influences of receptivity on turbulent transition by using a coupled compressible linearized Navier–Stokes (CLNS) and direct numerical simulation (DNS) framework to model the complete natural transition process. Leading-edge receptivity is naturally induced by freestream acoustic waves via CLNS, providing multi-mode solutions for downstream DNS. Investigating a subharmonic resonance, we compare natural scenario—incorporating continuous spectra and discrete modes—against a controlled scenario driven by an isolated Tollmien-Schlichting (TS) wave. The results demonstrate that the coalescence of various modes from the receptivity stage significantly accelerates the transition process. Notably, the natural scenario exhibits much earlier turbulent breakdown compared to the controlled scenario, even when the primary TS wave amplitudes are identical, due to enhanced parametric resonance induced by the coexisting modes. These findings emphasize that accurately predicting realistic natural transition requires incorporating receptivity physics rather than relying solely on the growth of discrete unstable modes.

Keywords: Receptivity, Boundary Layer Instability, Turbulent Transition, Computational Fluid Dynamics.

1. Introduction

Turbulent transition has been investigated for several decades due to its influence on drag and heat transfer on aircraft surfaces. Recently, numerous numerical studies have been conducted to predict turbulent transition. Most of them combine stability analysis, such as linear stability theory (LST), with high-fidelity simulations to calculate boundary layer transition efficiently [1, 2, 3, 4]. While successful, these methods are often limited to controlled transition scenarios because stability analysis is restricted to linear or weakly nonlinear growth regions. Crucially, most stability analysis methods calculate relative amplitudes, meaning the initial absolute amplitude is arbitrarily determined.

On the other hand, receptivity has been studied as a distinct branch of research. High-fidelity simulations or linearized equation methods have been applied to predict receptivity induced by acoustic [5, 6], vorticity [7], or entropy waves [7] at a leading edge [8, 9], local roughness [10], or shock [11]. However, most studies focusing on receptivity do not account for the growth of modes in nonlinear regions. Therefore, the effects of coexisting modes on turbulent transition remain under-investigated compared to transition triggered by a discrete unstable mode.

The growth of modes in weakly nonlinear regions in subharmonic resonance have been theoretically investigated using a resonant triad [12, 13, 14] and parametric resonance [15, 16, 4]. However, these works focused solely on several discrete modes, a fundamental planar wave and subharmonic oblique waves. As a result, interactions between coexisting modes associated with the fundamental wave, and their subsequent influence on subharmonic modes, remain not fully understood.

Some previous studies have explored influences of coexisting modes in transition [17, 18, 6]. Recently,

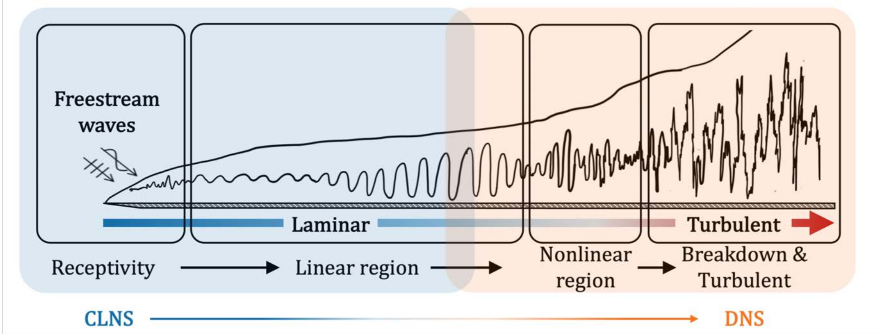

Figure 1: Schematic diagram of the current methodology.

Schuabb et al. [19] simulated full transition process in hypersonic flow. They considered entire process of natural transition using direct numerical simulation (DNS), which simulates transition triggered by broadband freestream acoustic disturbances. Simulations for full transition process are sectionally conducted because it is too large to be considered simultaneously. Computations were performed in sequential stages; the first simulation addressed receptivity, and subsequent simulations covered downstream regions. With validation against experimental results such as amplitude growth and spectra of pressure fluctuations, their computations successfully reproduced wind tunnel experiments. Despite these efforts, limited studies examine influences of coexisting modes, and underlying physics and mechanisms are not fully understood. Therefore, a detailed numerical investigation is further required to investigate influences of coexisting modes generated in receptivity to subsequent nonlinear breakdown.

To address the limitations of previous studies, the current study employs a compressible linearized Navier-Stokes (CLNS) method [11, 20] and high-fidelity simulation. The CLNS framework solves harmonic fluctuation equations without the additional assumptions often used in stability analysis, enabling the prediction of both receptivity and linear regions. Therefore, CLNS provides information on absolute amplitudes and results composed of various modes, including continuous spectra and discrete modes. Subsequently, direct numerical simulation (DNS) is applied to the downstream nonlinear regions and turbulent transition. This coupled CLNS-DNS approach captures every stage of natural transition—receptivity, linear growth, nonlinear breakdown, and turbulent transition—making it applicable to the entire transitional boundary layer.

In this study, we adopt flow conditions widely used in turbulent transition studies, specifically the subharmonic resonance scenario in low-speed flow [21, 1, 4]. However, instead of introducing artificial receptivity such as a blowing/suction slot or a vibrating ribbon inside the boundary layer, this study considers natural receptivity induced by freestream acoustic waves and the leading edge.

2. Methodology

The current methodology is illustrated schematically in Figure 1. In this study, two numerical methods are utilized to investigate natural transition, including receptivity. The CLNS method is applied to capture leading-edge receptivity and linear growth in the upstream regions. It provides disturbance information, such as mode shapes, for use in the subsequent high-fidelity simulation. DNS is then used to simulate the downstream region, resolving the remaining transition process and turbulent breakdown. While previous studies [1, 2, 4] used a similar approach, they excluded the receptivity stage. Consequently, their simulations were limited to controlled transition scenarios, focusing solely on the growth and interaction of major unstable discrete modes. In contrast, the current methodology incorporates receptivity, allowing for the consideration of multimodal effects that include both the continuous spectrum and discrete modes. This represents a more realistic scenario for natural transition process.

2.1 Receptivity and Primary Instability

A flow variable q can be decomposed into a mean part Q and a fluctuation part q'.

$$q = Q + q' \tag{1}$$

In laminar flow, the fluctuation can be expressed in a harmonic formulation.

$$q' = \hat{q} \exp\{i(\beta z - \omega t)\} \tag{2}$$

where β is a spanwise wavenumber and ω is an angular frequency. By substituting the given decomposition into the primitive Navier–Stokes equations and using the fluctuation ansatz, we can obtain the harmonic fluctuation equation. Early stages of transition, receptivity and linear regions (primary instability), are governed by linear equations; thus, the derived equation can be further simplified to a linearized equation. As a result, the linearized harmonic Navier–Stokes equations which are the governing equation of the CLNS method can be derived. The full equations can be found in the references [11, 20].

Since this study investigates turbulent transition initiated by freestream acoustic waves and the leading edge of a flat plate, a 2D planar freestream acoustic wave is introduced via the theoretical Euler equation at the far-field boundary in the CLNS computation. To minimize local scattering effects at the nose-body junction, a modified super-elliptic shape [8] is employed. The Reynolds number based on the plate half thickness and the aspect ratio are $Re_b = 2400$ and AR = 6. The nondimensional frequency of the acoustic wave is $F = \omega / Re_b \times 10^6 = 120$. Further detailed computational methods for the CLNS are provided in the reference [20].

To induce subharmonic resonance, we additionally need to obtain the subharmonic oblique wave. Here the subharmonic oblique wave with $\beta = 0.73$ is calculated by LST. It should be noted that the subharmonic oblique mode could also be calculated via CLNS to account for the receptivity process. However, the authors do not compute the subharmonic oblique mode using CLNS for two reasons. First, including it would complicate the analysis and obscure the underlying physics. Thus, the current study focuses only on the receptivity of the fundamental mode for clarity, which is the primary factor of subharmonic resonance.

Second, a subharmonic freestream acoustic wave which includes the subharmonic oblique mode would be an evanescent wave under the current flow conditions. A dispersion equation of the freestream acoustic wave which has zero incident angle can be written as Equation 3.

$$(\alpha_\infty U_\infty - \omega)^2 = (\alpha_\infty^2 + \beta_\infty^2) c_\infty^2 \tag{3}$$

where β_∞, α_∞, c_∞ are a spanwise wavenumber, streamwise wavenumber, and wave speed in freestream, respectively. In Equation 3, the only unknown variable is α_∞ so that the equation becomes the quadratic equation for α_∞. If the discriminant of this equation is negative, this wave is the evanescent wave. In this study, the given flow condition of the subharmonic freestream acoustic wave provides the negative discriminant so that this wave cannot reach the leading edge.

2.2 Secondary Instability and Turbulent Flow

For the complete transition simulation, the profiles obtained from the CLNS are imposed at the DNS inlet. Here the subharmonic resonance in low-$Mach$ flow is simulated using the proposed methodology. This resonance scenario has been widely investigated experimentally [23], theoretically [15, 16], and numerically [1, 2, 3, 4], though previous studies typically initiated it via artificial receptivity.

Following the CLNS calculation, three DNS cases are conducted with varying amplitudes for the fundamental mode. The profiles used in DNS are presented in Figure 2. In Figure 2a, the wall-normal component is magnified by a factor of 40 for visualization purposes. Unlike the $u'_{(2,0)}$ and $v'_{(2,0)}$ components of the TS wave in Figure 2b, the streamwise fluctuation $u'_{(2,0)}$ generated through receptivity

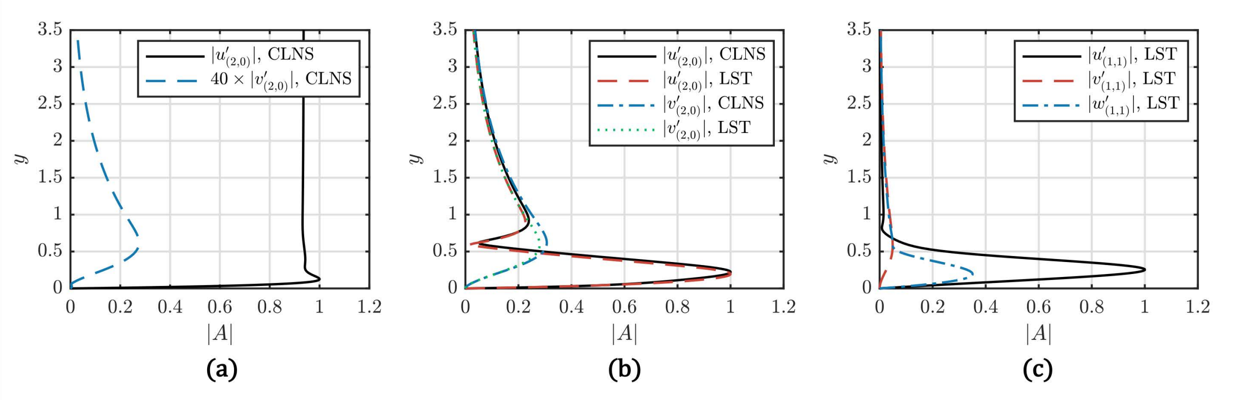

Figure 2: Amplitude profiles of (a) the fundamental mode generated through receptivity, (b) Tollmien-Schlichting (TS) wave, and (c) subharmonic oblique wave. All amplitudes are normalized by streamwise maximum amplitude, max $(|u'|)$.

is significantly stronger than $v'_{(2,0)}$ because it comprises a superposition of various modes. Figure 2b presents the profile of the TS wave extracted from the total CLNS results shown in Figure 2a. LST results are included solely for validation purposes. The TS wave profiles in Figure 2b are used for the CS case, while the total profiles in Figure 2a are used for the NS1 and NS2 cases. It is noteworthy that the $u'_{(2,0)}$ including various modes is 24.3 times larger than that of the TS wave, one discrete mode. The subharmonic oblique wave shown in Figure 2c is applied identically to all cases.

The magnitudes of the modes for each DNS case are summarized in Table 1. The CS case is used as the baseline, representing the controlled scenario investigated in previous studies. It employs the pure TS wave as the fundamental mode; thus, the amplitude of the fundamental mode is identical to that of the TS wave. The NS1 case uses the multi-mode solution—a summation of modes generated through receptivity—for the fundamental mode, rather than an isolated TS wave. Therefore, while it maintains the same TS wave amplitude as the CS case, the total amplitude of the fundamental mode is 24.3 times larger due to the contribution of the multi-mode solution in the CLNS results. The NS2 case uses the same profile as NS1 but with a reduced amplitude for the fundamental mode. For clarity, hereafter the fundamental mode and the isolated TS wave will be denoted as $u'_{(2,0)}$ and $u'_{(TS)}$, respectively. The subscript (m, n) indicates temporal harmonic modes and spanwise spatial harmonic modes of the subharmonic oblique mode $u'_{(1,1)}$.

$$u'_{(2,0)} = u'_{(TS)} + u'_{(others)} \quad \text{for NS} \tag{4a}$$
$$u'_{(2,0)} = u'_{(TS)} \quad \text{for CS} \tag{4b}$$

In contrast to the fundamental mode, the subharmonic oblique mode obtained using LST is consistent across all cases.

Table 1: Amplitudes of assigned modes at the inlet of DNS. The numbers in parentheses refer to TS wave amplitude included in the fundamental mode.

	Fundamental mode $u'_{(2,0)}$	Fundamental mode $u'_{(TS)}$	Subharmonic oblique mode
CS case	-	4×10^{-3}	2×10^{-5}
NS1 case	$24.3 \times 4 \times 10^{-3}$	(4×10^{-3})	2×10^{-5}
NS2 case	4×10^{-3}	$(4 \times 10^{-3}/24.3)$	2×10^{-5}

The computational domain of DNS is in $400 \leq \sqrt{Re_x} \leq 1000$, and 64 streamwise grid points are allocated per wavelength of TS wave. The first wall normal grid size y_1^+ is less than 0.1 in the entire domain since

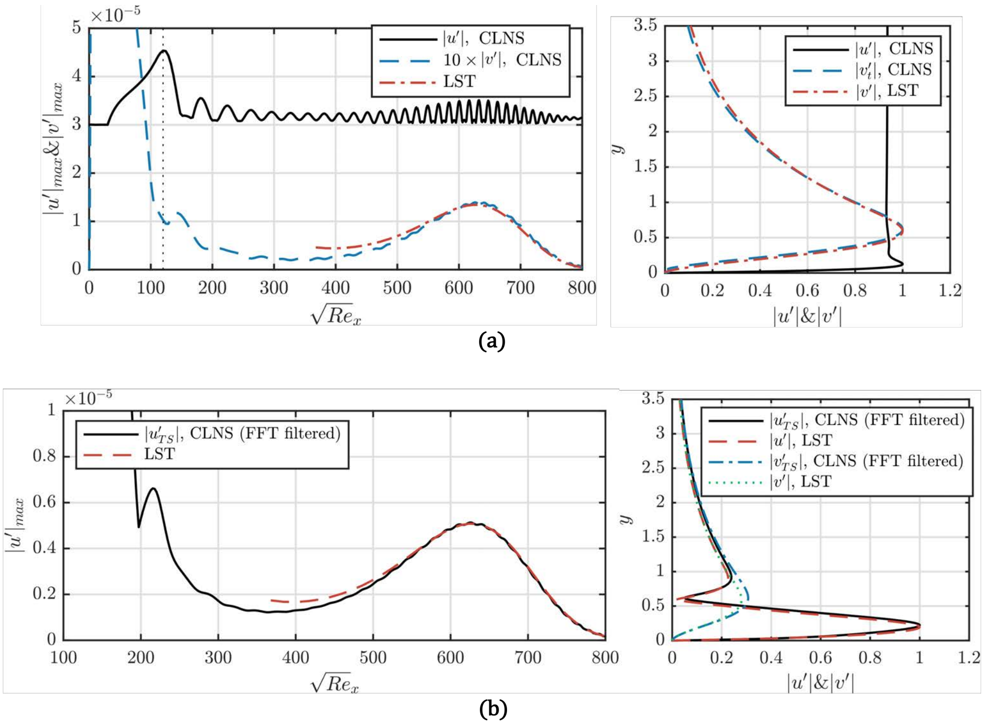

Figure 3: Maximum amplitude growth and mode shapes of u' and v' at $\sqrt{Re_x} = 400$ (branch I). (a) CLNS results without the extraction method and (b) CLNS results with the TS wave extraction method. Adapted from [20].

DNS shares the wall-normal distribution with the CLNS simulation. In spanwise direction, 32 grid points are distributed per spanwise wavelength oblique modes, which was shown to be sufficient to capture turbulent transition in the previous study [24, 3]. Further detailed computational methods used in DNS are provided in the reference [24].

3. Computational Results

In the current study, CLNS and DNS are used to simulate turbulent transition in boundary layer induced by the artificial receptivity and natural receptivity. For complete simulation in DNS, CLNS provides the multi-mode profile as well as the TS wave and LST provides the subharmonic mode.

Brief results of receptivity and linear regions simulation are provided in Figure 3 to validate the current CLNS solver. Without any post-processing, the amplitude growth of u' along $\sqrt{Re_x}$, the Reynolds number based on the streamwise distance, remains nearly constant because of freestream acoustic wave as shown in Figure 3a. Due to modes in boundary layer, some oscillations exist. On the other hand, the wall normal component agrees well with LST results. The mode shapes of v' from CLNS and LST are also well overlapped. Streamwise component u', however, has the mode shape similar to the Stokes layer profile rather than TS wave shown in Figure 3b. To compare the streamwise components with LST for further validation, we need to extract TS wave in the coexisting modes that share the same frequency as the TS wave but differ in spatial wavelength. Following previous studies [22, 20], two step procedures consisting of subtraction of a Stokes wave followed by a filtering method are applied. The extracted TS wave of CLNS is comparable to LST results as shown in Figure 3b so that the current CLNS code and obtained results are successfully validated.

The current DNS is also validated with previous studies using maximum amplitude growth in Figure 4. Since previous studies have focused on the controlled scenario transition, CS is used for comparison. In Table 2, initial amplitudes of the fundamental and subharmonic modes previous and current computations

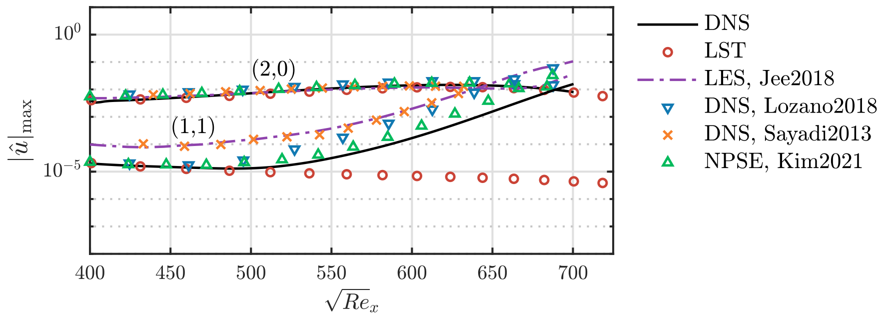

Figure 4: Maximum amplitude growth of TS wave $(2, 0)$ and subharmonic oblique wave $(1, 1)$. Results of current DNS (CS) and LST [25] are compared with previous LES, DNS, and NPSE. NPSE [4] was conducted with $\Delta\phi_{in} = 40°$.

are summarized. All simulations directly assigned the fundamental and subharmonic modes at the inlet except Sayadi et al. [21]. They used a wall blowing/suction method to generate TS wave and subharmonic oblique wave in boundary layer so that their initial amplitudes cannot be directly compared with other studies. It is noteworthy that different amplitudes in TS wave will induce different growth of the subharmonic mode. The current DNS uses a weaker amplitude than previous studies so that growth of the subharmonic mode can be delayed compared to other studies.

Table 2: Initial maximum amplitudes of TS wave and the subharmonic mode in previous [2, 1, 21, 4] and current computations.

	Fundamental mode	Subharmonic oblique mode
Current DNS (CS)	4×10^{-3}	2×10^{-5}
LES, Jee et al. [2]	6.5×10^{-3}	1.4×10^{-4}
DNS, Lozano et al. [1]	6.8×10^{-3}	2.1×10^{-5}
DNS, Sayadi et al. [21]	3×10^{-3}	1.5×10^{-5}
DNS, Kim et al. [4]	5.7×10^{-3}	2.3×10^{-5}

Despite different initial amplitudes of TS wave $(2, 0)$, growth of TS wave from the current DNS and previous studies agrees well. However, the subharmonic oblique mode $(1, 1)$ presents a large variation among the studies due to different initial amplitudes of TS wave. LES by Jee et al. [2] and DNS by Sayadi et al. [21] are comparable while other studies provide one order of magnitude smaller subharmonic amplitude.

DNS by Lozano-Duran et al. [1] and nonlinear parabolized stability equations (NPSE) [4] used the similar initial amplitudes with the current DNS results so that subharmonic growth in the current DNS is close to their results. However, the point where the subharmonic grows rapidly (exponentially) is different between DNS, NPSE, and the current study. This discrepancy can be caused by different initial amplitudes of TS wave. Additionally, it might be also induced by $\Delta\phi_{in}$ which is the initial phase difference between TS wave and subharmonic oblique waves. Kim et al. [4] demonstrated that the initial phase difference $\Delta\phi_{in}$ between TS wave and subharmonic oblique waves can change interactions between those modes. They also showed that transition onset and turbulent transition can be largely varied by $\Delta\phi_{in}$ using NPSE and LES. Consequently, we can explain discrepancies in growth of the subharmonic mode by influences of different initial amplitudes of TS wave and initial phase differences $\Delta\phi_{in}$.

Averaged skin friction coefficient in the current DNS is also compared with previous studies in Figure 5. Both CS and NS cases are plotted here. The current DNS simulations show low C_f in turbulent flow due to relatively coarse resolution in spanwise direction. However, the previous studies [26, 3] which used a coarse grid resolution already demonstrated that the current spatial resolution is enough to predict

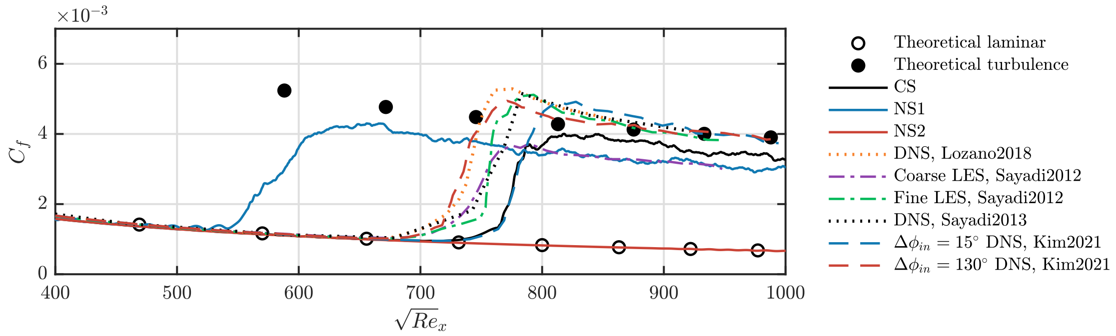

Figure 5: Averaged skin friction coefficients C_f along streamwise direction. [25].

transition. This is also shown in Figure 5. Coarse LES (purple dashed-dot line) [26] predicts low C_f, similar to the current DNS C_f in turbulent boundary layer, while Sayadi et al. [26] successfully predicted amplitude growth before transition with this coarse grid. Similarly, transition location from coarse LES C_f is comparable to fine LES (green dashed-dot line) and DNS (black dotted line) until $\sqrt{Re_x} = 750$.

On the other hand, CS case shows turbulent transition near $\sqrt{Re_x} = 750$ where locates slightly downstream compared to other previous studies except DNS from Kim et al. [4]. As discussed in maximum amplitude growth comparison, this difference can be induced by effects of $\Delta\phi_{in}$. DNS with $\Delta\phi_{in} = 130°$ [4] shows identical transition location to other DNS studies, while DNS with $\Delta\phi_{in} = 15°$ [4] predicts delayed transition location. The current CS are very well agreed to DNS with $\Delta\phi_{in} = 15°$. This result confirms that discrepancies in maximum amplitude growth and skin friction evolution are due to different initial amplitudes and $\Delta\phi_{in}$, not numerical errors. NS1 which uses receptivity-generated multi-mode solution as the fundamental mode predicts transition upstream $\sqrt{Re_x} = 550$ compared to CS. In contrast, NS2 C_f continuously follows theoretical laminar C_f meaning no transition in NS2.

To visualize the growth of instability modes and turbulent transition, the vortical structures are presented in Figure 6. Although the multi-mode profile is imposed at the inlet for the NS1 case, the resulting vortical structures are qualitatively similar to those of the CS case. Both cases initially exhibit 2D vortical structures, followed by the emergence of 3D structures further downstream due to modal interactions. Specifically, Staggered-Λ vortices are clearly evident in both cases. The primary difference lies in the breakdown location of large-scale structures, which occurs significantly farther upstream in the NS1 case compared to the CS case. This indicates that transition is triggered earlier in NS1 which is consistent with skin friction evolution, despite both cases sharing the same TS wave amplitude.

For the NS2 case, vortical structures are visualized using a lower Q-criterion threshold than in the other two cases. Despite having the same total fundamental amplitude as the CS case, the NS2 case exhibits significantly delayed growth due to the weaker TS wave component. This weaker TS wave is insufficient to trigger the rapid growth of the subharmonic oblique mode observed in the CS and NS1 cases. Consequently, turbulent transition does not occur in the NS2 case within the computational domain.

The amplitude growth of the three cases are compared to investigate the evolution of the instability modes. For the NS cases, the TS wave extraction method is applied to obtain $\hat{u}_{(TS)}$, while the CS case does not require this procedure because the TS wave is inherently isolated. Therefore, only the fundamental mode, which is identical to the TS wave in the CS case, is illustrated in Figure 7a. The TS waves in all cases agree well with the LST predictions; thus, it can be conjectured that the coexisting modes within the fundamental wave remain decoupled in the nonlinear regions, just as they do in the linear regions.

In the CS case, the subharmonic mode initially follows the LST prediction and increases rapidly starting from $\sqrt{Re_x} = 500$. In contrast, the subharmonic mode in the NS1 case begins to grow much more rapidly from further upstream. Since the amplitudes of the primary TS waves in both the CS and NS1 cases are nearly identical, the accelerated subharmonic growth in the NS1 case can be attributed to the influence of the coexisting disturbances.

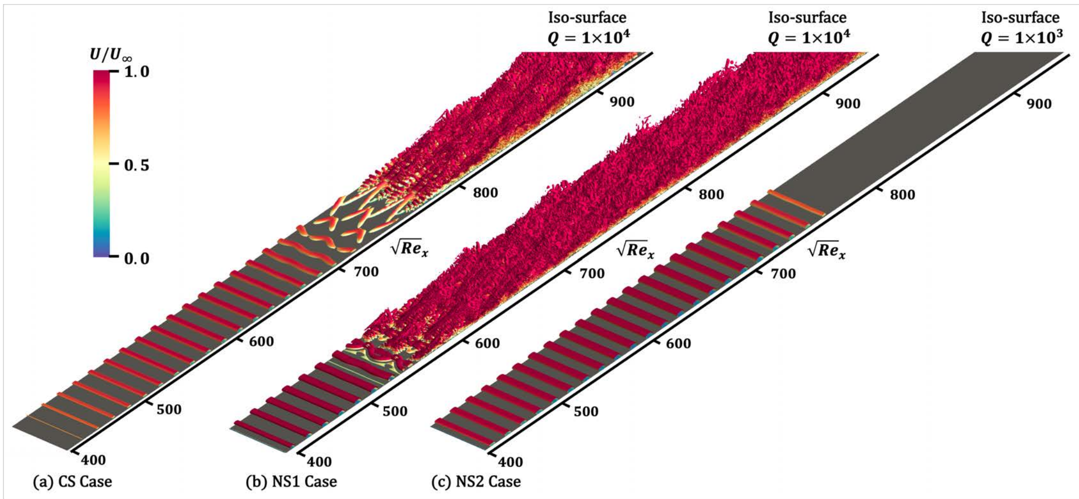

Figure 6: Vortical structures visualized by iso-surface of Q-criterion colored by streamwise velocity. Computational results are duplicated in the spanwise direction for clear visualization. Threshold values of Q for each cases are indicated at the top of figures [25].

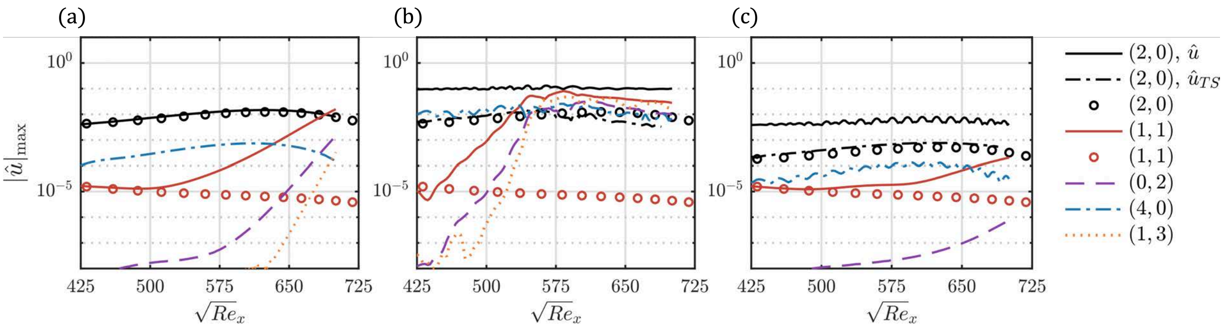

Figure 7: Maximum amplitude growth of instability modes along streamwise directions. (a) CS case, (b) NS1 case, and (c) NS2 case. [25]

In the NS2 case, the subharmonic mode initially decays; however, it soon departs from the LST results and exhibits slow growth, which not shown in typical subharmonic resonance process. Previous study [4] has shown that a TS wave with a low amplitude of $A_{TS} \leq O(10^{-4})$ cannot induce subharmonic growth. Although the TS wave amplitude in the NS2 case is also $A_{TS} \leq O(10^{-4})$, the subharmonic mode still grows. This indicates that the coexisting modes among the fundamental wave affect the subharmonic mode. However, unlike TS wave, the coexisting modes cannot induce subharmonic resonance with the subharmonic mode; consequently, $\hat{u}_{(1,1)}$ grows slowly rather than exponentially.

A key finding of this study is that transition is not solely governed by discrete unstable modes such as the TS wave, but is substantially altered by the coexisting modes in the fundamental mode introduced through natural receptivity. Previous transition analyses, which typically consider only a few discrete modes, have been successful in explaining well-established mechanisms such as parametric resonance, phase-locking conditions, and resonant triads. However, the present results reveal that additional modes generated during the receptivity stage further enhance secondary instability beyond what is attributable to the TS wave alone. Consequently, turbulent breakdown in the natural scenario occurs significantly earlier than in the controlled scenario, highlighting the necessity of accounting for receptivity when modeling realistic boundary-layer transition.

The mode shapes at three streamwise locations are presented in Figure 8. In upstream region, mode shapes of three cases are comparable, supporting validity of the current TS wave extraction method.

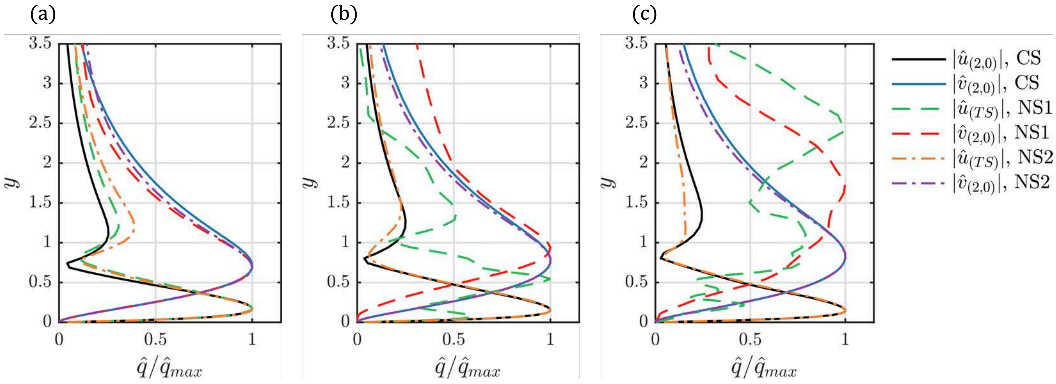

Figure 8: Mode shapes of TS wave in three cases at (a)$\sqrt{Re_x}$ = 480, (b)$\sqrt{Re_x}$ = 570, and (c)$\sqrt{Re_x}$ = 640 [25].

However, NS1 provides distorted shapes because turbulent transition already occurs in this location. Its shape becomes more distorted in further downstream since the flow is evolved into fully developed turbulent boundary layer. In contrast, CS and NS2 are consistently comparable in downstream locations since transition in CS occurs near $\sqrt{Re_x}$ = 750 and NS2 does not provide transition.

4. Conclusion and Future Work

A CLNS-DNS framework was used to simulate the complete natural transition process. This study used the CLNS method to calculate receptivity, and subsequent DNS was carried out in downstream. Comparisons between natural (receptivity-generated multimodes) and controlled (discrete-mode only) scenarios revealed that the coalescence of various modes accelerates transition process. Specifically, the natural scenario exhibited earlier breakdown than the controlled scenario, even when the primary unstable mode amplitude was matched. Consequently, relying solely on discrete mode growth is insufficient; incorporating receptivity physics is essential for accurate transition prediction.

These findings provide valuable insights into realistic transition processes governed by multi-modal interactions. To rigorously elucidate the physical mechanisms underlying this mode coalescence, theoretical approaches are necessary. In future work, secondary instability analysis—such as employing a modified Floquet theory that incorporates Stokes layer effects into the base flow—will be conducted to precisely identify the fundamental sources driving the enhanced growth of the subharmonic mode.

Acknowledgements

This study was supported by the Korea Institute of Science and Technology Information (KISTI)(No. K26L1M2C3). Computational resources and technical support were provided by the National Supercomputing Center (Project Number KSC-2024-CRE-0250).

References

[1] A. Lozano-Durán, M. J. P. Hack, and P. Moin. Modeling boundary-layer transition in direct and large-eddy simulations using parabolized stability equations. *Physical Review Fluids*, 3:023901, 2018.

[2] Solkeun Jee, Jongwook Joo, and Ray-Sing Lin. Toward Cost-Effective Boundary Layer Transition Computations With Large-Eddy Simulation. *Journal of Fluids Engineering*, 140(11):111201, 2018.

[3] Minwoo Kim, Jiseop Lim, Seungtae Kim, Solkeun Jee, and Donghun Park. Assessment of the wall-adapting local eddy-viscosity model in transitional boundary layer. *Computer Methods in Applied*

Mechanics and Engineering, 371:113287, 2020.

[4] Minwoo Kim, Seungtae Kim, Jiseop Lim, Ray-Sing Lin, Solkeun Jee, and Donghun Park. Effects of phase difference between instability modes on boundary-layer transition. *Journal of Fluid Mechanics*, 927:A14, 2021.

[5] William Saric and Edward White. Influence of high-amplitude noise on boundary-layer transition to turbulence. In *29th AIAA Fluid Dynamics Conference*, 1998. AIAA 98-2645.

[6] P. Balakumar and Amanda Chou. Transition Prediction in Hypersonic Boundary Layers Using Receptivity and Freestream Spectra. *AIAA Journal*, 56(1):193–208, 2018.

[7] Alexander V Fedorov and Natalia Palchekovskaya. Receptivity of high-speed boundary layer on a flat plate at angles of attack: entropy and vorticity waves. *Theoretical and Computational Fluid Dynamics*, 37(5):549–558, 2023.

[8] Nay Lin, Helen L Reed, and WS Saric. Effect of leading-edge geometry on boundary-layer receptivity to freestream sound. In *Instability, Transition, and Turbulence*, pages 421–440. Springer, 1992.

[9] Nima Shahriari, Daniel J Bodony, Ardeshir Hanifi, and Dan S Henningson. Acoustic receptivity simulations of flow past a flat plate with elliptic leading edge. *Journal of Fluid Mechanics*, 800:R2, 2016.

[10] Lei Zhao and Ming Dong. Effect of suction on laminar-flow control in subsonic boundary layers with forward-/backward-facing steps. *Physics of Fluids*, 32(5), 2020.

[11] Mujeeb Malik, Ray-Sing Lin, and Raja Sengupta. Computation of hypersonic boundary-layer response to external disturbances. In *37th AIAA Aerospace Sciences Meeting and Exhibit*, 1999. AIAA 1999-411.

[12] Alex DD Craik. Non-linear resonant instability in boundary layers. *Journal of Fluid Mechanics*, 50(2):393–413, 1971.

[13] Reda R Mankbadi, Xuesong Wu, and Sang Soo Lee. A critical-layer analysis of the resonant triad in boundary-layer transition: nonlinear interactions. *Journal of Fluid Mechanics*, 256:85–106, 1993.

[14] Xuesong Wu, Sangsoo Lee, and Stephen J Cowley. On the weakly nonlinear three-dimensional instability of shear layers to pairs of oblique waves: the Stokes layer as a paradigm. *Journal of Fluid Mechanics*, 253:681–721, 1993.

[15] Thorwald Herbert. Analysis of the subharmonic route to transition in boundary layers. In *22nd aerospace sciences meeting*, page 9, 1984.

[16] AH Nayfeh and JA Masad. Recent advances in secondary instabilities in boundary layers. *Computing Systems in Engineering*, 1(2-4):401–414, 1990.

[17] Tamer A Zaki and Paul A Durbin. Mode interaction and the bypass route to transition. *Journal of Fluid Mechanics*, 531:85–111, 2005.

[18] YANG Liu, Tamer A Zaki, and Paul A Durbin. Boundary-layer transition by interaction of discrete and continuous modes. *Journal of Fluid Mechanics*, 604:199–233, 2008.

[19] Mateus Schuabb, Lian Duan, Katya M Casper, Ross M Wagnild, Meelan M Choudhari, and Pedro Paredes. Hypersonic boundary-layer transition over a circular cone in a Mach 8 digital wind tunnel. *Journal of Fluid Mechanics*, 1017:A33, 2025.

[20] Minwoo Kim and Ilyoup Sohn. Numerical study on leading-edge receptivity of acoustic waves in subsonic flow utilizing compressible linearized Navier–Stokes method. *AIP Advances*, 16(2), 2026.

[21] Taraneh Sayadi, Curtis W. Hamman, and Parviz Moin. Direct numerical simulation of complete H-type and K-type transitions with implications for the dynamics of turbulent boundary layers. *Journal of Fluid Mechanics*, 724:480–509, 2013.

[22] MR Turner. Tollmien–Schlichting wave amplitudes on a semi-infinite flat plate and a parabolic body: comparison of a parabolized stability equation method and direct numerical simulations. *Quarterly journal of mechanics and applied mathematics*, 65(2):183–210, 2012.

[23] Yu S Kachanov and V Ya Levchenko. The resonant interaction of disturbances at laminar-turbulent transition in a boundary layer. *Journal of Fluid Mechanics*, 138:209–247, 1984.

[24] Minwoo Kim, Jiseop Lim, Seungtae Kim, Solkeun Jee, Jaeyoung Park, and Donghun Park. Large-eddy simulation with parabolized stability equations for turbulent transition using OpenFOAM.

Computers & Fluids, 189:108–117, 2019.

[25] Minwoo Kim and Ilyoup Sohn. Effects of leading-edge receptivity on subharmonic resonance transition in boundary layer. *Journal of Fluid Mechanics*, preparing, 2026.

[26] Taraneh Sayadi and Parviz Moin. Large eddy simulation of controlled transition to turbulence. *Physics of Fluids*, 24(11):114103, 2012.